LIMNOLOGY
and
OCEANOGRAPHY: METHODS

Limnol. Oceanogr.: Methods 8, 2010, 254–268

A novel planar optode setup for concurrent oxygen and light field imaging: Application to a benthic phototrophic community

Jan P. Fischer and Frank Wenzhöfer*
Max Planck Institute for Marine Microbiology, Celsiusstrasse 1, 28359 Bremen, Germany

Abstract

A novel high resolution planar optode (HiPO) for two dimensional oxygen and light-field imaging is presented. Optical cross-talk effects, limiting the precision and resolution of conventional planar optode setups, could be strongly reduced by the use of a fiber optic faceplate as sensing window. The new device, therefore, allows for accurate calculation of oxygen fluxes and respiration rates from oxygen concentration images, especially for measurements on small scales. In addition, the setup can be used to estimate the distribution of scalar irradiance within illuminated sediments or mats, thus directly linking local light availability to oxygen dynamics at high resolution. Irradiance values obtained with the HiPO were found to be in good agreement with scalar irradiance microsensor measurements in sandy sediment, and a spatial resolution of ~120 µm could be achieved. The performance of the HiPO for oxygen measurements was tested experimentally and the theoretical limit of spatial (~100 µm) and temporal (~10 s) resolution, governed by oxygen diffusion within the sensing layer, was determined by mathematical modeling. Rates of primary production and respiration in sandy sediments were calculated from the transient oxygen concentrations after perturbations in light condition showing a highly patchy distribution on submillimeter scale. These heterogeneities were clearly correlated to local irradiance within the sediment. Spatial correlations of photosynthesis and respiration were strongly dependent on incident irradiance.

The dynamic change of oxygen concentrations within sediments and microbial mats contains information about oxygen-consuming processes (e.g., carbon mineralization) and benthic primary production, and has therefore been widely studied for decades (e.g., Pamatmat 1971; Hargrave 1972; Jørgensen and Revsbech 1985). In many phototrophic ecosystems like microbial mats or coastal sediments, the availability of light is the major driving force of benthic oxygen dynamics since the activity of primary producers depends on the local availability of light to the organisms within the sediment strata (Jørgensen and Des Marais 1986). The light field within sediments exhibits a great spatial (vertical penetration of light, lateral differences due to inhomogeneities in the sediment) and temporal (e.g., dial light cycle, clouds, surface waves) variability, often causing small-scale heterogeneities in zones of oxygen production and consumption (Glud et al. 1999; Glud 2008). Lassen et al. (1992b) and Dodds (1992) introduced microscale sensors with a close to spherical light acceptance characteristic, using a scattering translucent sphere with a diameter between 70 and 250 µm glued to the end of a light guiding fiber. These sensors allow measurements of scalar irradiance, i.e., the integrated light from all directions that is available for algal cells (Kühl and Jørgensen 1992).

To assess the vertical organization of gross photosynthesis, Revsbech et al. (1981) introduced the light–dark shift method. They recorded the initial decline in oxygen concentration over ~1 s immediately after a sudden darkening of the sediment using fast responding microelectrodes (Revsbech and Jorgensen 1983). Under the assumption of initially unchanged respiration rate and diffusion, the rate of oxygen disappearance in the dark is equal to the photosynthesis rate in the light. By repeating this measurement scheme in different sediment depth, profiles of benthic gross photosynthesis can be determined, which is a time-consuming procedure. Fitting a polynomial to the decrease in oxygen concentration over a longer time of 4 s revealed that the linear fit method most likely underestimates gross photosynthesis (Lassen et al. 1998). A more sophisticated approach addresses changes in

*Corresponding author: Email: jfischer@mpi-bremen.de;
Phone: ++ 49(0)421-2028-877

Acknowledgments

We are grateful for assistance with the calculations of Dieter Wolf-Gladrow, helpful discussions with Arzhang Kalili, and valuable comments from Rita Dunker. Ronnie N. Glud and one anonymous reviewer helped to improve the manuscript. This research was supported by the Max Planck Society.

DOI 10.4319/lom.2010.8.254

diffusive oxygen flux by mathematical modeling of the reaction-diffusion equation and iterative comparisons with measured oxygen profiles (Revsbech et al. 1986). Epping et al. (1999) measured profiles of benthic photosynthesis and respiration rates in sediments, combining oxygen measurements and numerical simulations of the transient oxygen field after changing the light conditions (light–dark cycle method). While also based on perturbations in the light condition, this method does not only consider the first few seconds after darkening but can follow changes in community respiration over time. To study the relation between local light availability and gross photosynthesis at the respective depths, scalar irradiance microsensors and the light–dark shift method have been used together by Lassen et al. (1992a). They found that the horizontal distance of 120 µm between the tip of oxygen and light microsensors resulted in an uncertain relationship between the two measured parameters in individual profiles.

It is known that the lateral heterogeneity within sediments and microbial mats can be very high (Revsbech and Jørgensen 1983; Wenzhöfer and Glud 2004; Stockdale et al. 2009). To approach the whole, three-dimensional (3D) dynamic picture in sediments and microbial mats, planar optodes (PO) have been introduced to the field of marine research (e.g., Glud et al. 1996). This imaging technology allows mapping oxygen distributions and their change over time and has become an important tool in marine research. Main part of the "conventional" system is a transparent support foil with a fluorescent coating, which changes fluorescence intensity and lifetime depending on the oxygen concentration (Holst et al. 1998). Planar optodes have been applied in numerous studies and in many different habitats like coastal sands (Glud et al. 2001; Wenzhöfer and Glud 2004; Franke et al. 2006; Behrens et al. 2007), deep-sea sediments (Glud et al. 2005), microbial mats (e.g., Glud et al. 1999), rhizospheres (Jensen et al. 2005; Frederiksen and Glud 2006), and endolithic algal communities (Kühl et al. 2008). First used in the laboratory, this technology was later also incorporated into in situ modules to study shallow water (Glud et al. 2001) and deep-sea (Glud et al. 2001; Glud et al. 2005) sediments under natural conditions. Subsequent modifications of the imaging technology, using lifetime imaging rather than intensity (Holst et al. 1998), and also of the sensor chemistry (e.g., König et al. 2005) further improved the solute imaging. Holst et al. (2001) used a transparent PO to image the structures behind the Optode together with the oxygen distributions. Recently, a special setup for low oxygen concentrations was developed (Oguri et al. 2006) and planar optodes were used together with hyperspectral imaging of pigments (Bachar et al. 2008; Kühl and Polerecky 2008).

Glud et al. (1999) combined light–dark shift measurements with microsensors with planar optode technology to assess two-dimensional (2D) distributions of respiration rates and photosynthesis and found pronounced small-scale variability in respiration and production. They calculated the second spatial derivative of an oxygen image to obtain the data. However, this approach needs some caution, since noise in the image is being strongly amplified by derivation. Smoothing and pixel averaging is required with concurrent loss of spatial resolution and inherent underestimation of calculated rates.

The benefit of imaging technologies is obvious in spatially heterogeneous systems like microbial mats or sediments, which are intensely influenced by bioturbation or bioirrigation. However, also in cases where the oxygen distribution is rapidly changing, the use of POs can be superior over profiling methods using microelectrodes or fiber optodes because the time required to get one microsensor profile is in the order of 15–30 min. In contrast, recording one oxygen image with a PO setup (comprising hundreds of profiles) is done typically in less than 1 s. Hence, it is possible to obtain time series of oxygen images in high frequency. However, the response time of the sensing foil itself may be in the order of 10–20 s, which is too slow to apply the light–dark shift method, where response times below 1 s are desirable (Revsbech and Jørgensen 1983).

Recent studies showed that the accuracy of conventional PO measurements on small scales and in high gradients is reduced by an optical cross-talk effect in the window and the support foil of the PO (Franke 2005). Values in the oxic regions are underestimated and oxygen gradients in the oxic/anoxic transition zone are flattened. This decreases the significance of measured fluxes and respiration rates, especially if the heterogeneity on small scales is high. Another resolution-limiting factor for PO measurements that is evaluated in this study is the diffusion of oxygen within the sensing layer and support foil. Recently, Kühl et al. (2007) presented a PO system for simultaneous microscopic imaging of biofilms and oxygen concentrations. They addressed this problem by decreasing the thickness of the sensing layer to 1-2 µm. This system, however, is restricted to artificial biofilms on microscopic slides. Lately, Mayr et al. (2009) reported the use of antenna pigments to enhance the brightness of luminescent sensors, a principle that could be used to decrease the sensor thickness and construct fast optodes for larger areas.

The light-guidance effect within the sensor foil and window not only limits the resolution of PO measurements, it also prevents the accurate imaging of light fields in sediments or microbial mats which are illuminated from the top. Here, we describe and demonstrate a new type of planar optode setup for high resolution analysis of oxygen concentration distributions as well as light intensities, using a fiber optic faceplate. The system allows correlating oxygen distributions with estimates of locally available irradiances. Sensor characteristics such as response time and spatial resolution were assessed, and the acceptance angle for local light-field measurements was determined. Two-dimensional light-field data were compared with profiles obtained with a scalar irradiance microsensor. To calculate rates of benthic photosynthesis and respiration, we adapted the light–dark cycle method of Epping et al. (1999), combining oxygen measurements with numerical simulation of the diffusion equation for 2D. The system was

applied to sandy sediments and the data are discussed with special focus on spatial heterogeneity.

Materials and procedures

Manufacturing the high resolution planar optode (HiPO)—In contrast to the conventional PO, using a polymer support foil, the HiPO described here consists of an oxygen sensitive layer, coated directly onto a fiber optic faceplate (FOFP) (SCHOTT North America; Fig. 1b). The FOFP itself was custom-made from light guiding glass fibers, which are fused together perpendicular to the surface of the plate with the dimensions 50 mm × 50 mm × 10 mm (Fig. 1b). Each single fiber has a core diameter of 6 µm with a center-to-center distance of 10 µm. The space between the fibers is filled with black light–absorbing glass. This assembly leads to the transportation of an image from one side of the plate, pixel by pixel, to the other. The FOFP is therefore an optically anisotropic material, where light guidance is only possible perpendicular to the plane surfaces.

The oxygen-sensing layer consisted of platinum(II)mesotetra (pentafluorophenyl)porphyrin (Frontier Scientific) dissolved together with polystyrene in chloroform according to the protocol of Precht et al. (2004). To increase the amount of excitation light within the sensing layer, titanium dioxide particles (5 µm, Aldrich) were added (König et al. 2005). These particles do not interfere with the quenching, but enhance the signal by scattering up to 10-fold, depending on their concentration (Zhou et al. 2007). While not mandatory for oxygen measurements, they strongly widen the acceptance angle for light-field measurements. The fluorophore was applied by knife coating with a gap of 50 µm (KControl Coater, RK Print Coat Instruments). After slow evaporation of the chloroform, the resulting sensing layer (phorphyrin in polystyrene matrix) had a thickness of 15–20 µm.

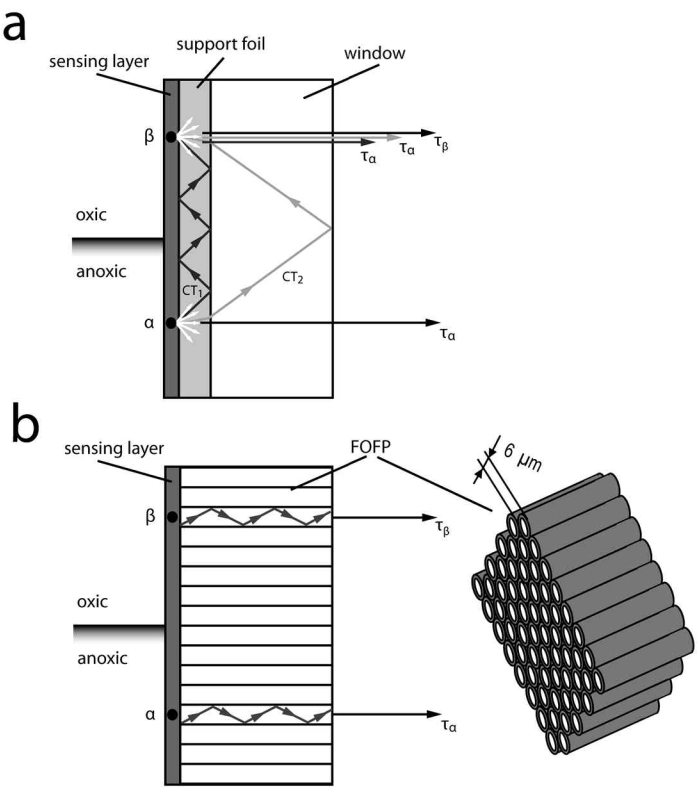

Fig. 1. (a) Cross-section of the conventional planar optode. Light traveling within the support foil (CT_1) and the window (CT_2) leads to optical cross-talk and mixing of fluorescence information. Light with the lifetime τ_α therefore also contributes to the fluorescence, measured for point β (modified after Franke 2005). (b) Cross-section through the High Resolution Planar Optode (HiPO). A Fiber Optic Faceplate (FOFP), consisting of millions of light-guiding fibers prevents optical cross-talk. The dimension of the plate itself is 50 mm × 50 mm × 10 mm. The diameter of the single fibers is 6 µm; the distance between the centerlines of the fibers is 10 µm.

Flow-through aquarium and HiPO setup—The FOFP was fitted into an aperture in a wall of a small polystyrene box (20 cm × 10 cm × 8 cm), with the sensing layer facing inside and flush with the aquarium wall (Fig. 2). The box was designed like a small flume with inlet and outlet in the short side walls and flow-laminarizing honeycomb structures on both sides for experiments with sandy sediments and microbial mats. A small aquarium pump circulated the seawater, using a 10-L container as reservoir. To prevent porewater advection in the permeable sandy sediment, the sediment topography was flat and the flow rate was adjusted to a minimum, necessary to create a stable diffusive boundary layer. The fluorophore of the HiPO was excited with 2 blue LEDs with collimating optics (LUXEON Star Royal Blue 5W LXHL-MRRC, peak wavelength 455 nm, Lumiled™) regulated by a homemade fast switchable current source (adjustable between 10 mA and 1000 mA). The emitted red luminescent light (λ_{max} = 647 nm) was imaged with a peltier-cooled, highly sensitive, fast gateable, 12 bit b/w, 1280 × 1024 pixel CCD camera (SensiMod, PCO Computer Optics) with a macro objective (SKR Componon 12 35/2.8, Stemmer Imaging). The objective was chosen to ensure a distortion-free projection of the image with a small object-to-objective distance to keep the setup compact (Fig. 2). A long-pass filter (Kodak red wratten gelatin filter Nr. 29 [deep-red], Kodak, cutoff wavelength ~580 nm) was installed between the objective and the CCD chip of the camera to block all blue light from the LEDs. This setup allowed distortion-free imaging with a resolution down to 5 µm pixel^{-1}. A homemade trigger source was used to synchronize camera and LED excitation. Illumination of the sediment (to stimulate photosynthesis) was switched off for < 1 s during the oxygen concentration imaging to avoid interferences with the light field. A lifetime-based measuring scheme was applied for the calculation of the oxygen field in front of the HiPO (Holst et al. 1998). Assuming a mono-exponential decay of the luminescence, the fluorescence lifetime can be calculated for each pixel. The resulting lifetime image was calibrated into an oxygen image using a modified version of the Stern-Vollmer equation, assuming a fraction of nonquenchable fluorescence of 0.15, which has been found typical for this sensing complex (e.g., Holst and Grunwald 2001). An area-averaging 2-point

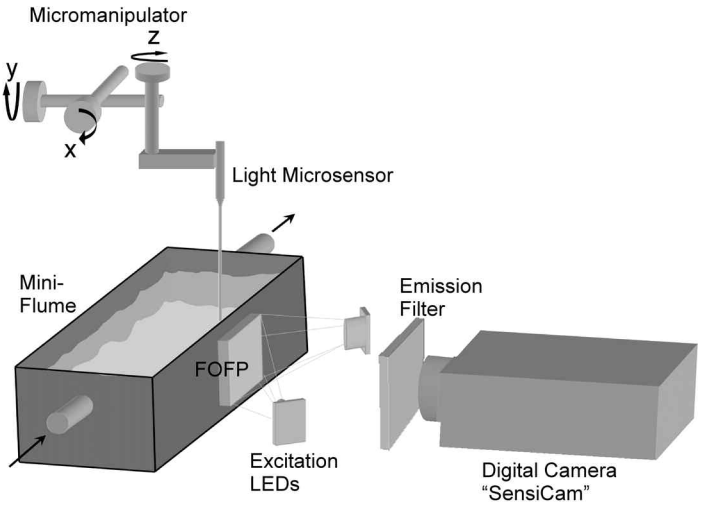

Fig. 2. Setup of HiPO. A fiber optic faceplate inserted in a miniaturized flume and coated with a fluorophore is illuminated by blue LEDs. The resulting fluorescence is recorded with a specialized camera system. A micromanipulator is used to position a scalar irradiance microsensor for calibration of the light measurements with the HiPO.

calibration at 0% oxygen and air saturation was carried out (Glud et al. 1996). Pixel-to-Pixel calibration was not necessary, since sensing layer and excitation light was very homogeneous and lifetime imaging was used. Image acquisition and trigger control were performed with custom-made software (Look@Molli v1.84). The subsequent image analyses and the calculations of lifetime and oxygen images were done with homemade software using MATLAB 6.5 (MathWorks).

Light-field measurements—Above the flume, a line of 4 white power LEDs (LUXEON Star Warm White, 1 W, LXHL-MWGC) with collimating optics was mounted to create a homogeneous light field at the surface of the sediment, stimulating benthic photosynthesis. These LEDs emit a continuous spectrum from ~400 nm to ~780 nm. Compared with sunlight, the LED spectrum contains virtually no UV- and IR-light. The peak wavelength of 630 nm is higher compared with 520 nm of sunlight (Luxeon technical data sheet DS47, www.philipslumileds.com/pdfs/DS47.pdf). However, the LED spectrum is closer to natural conditions than most other artificial light sources. The irradiance at the sediment surface was adjusted from 0 to ~300 µmol photons m^{-2} s^{-1} as measured with a spherical quantum sensor (US-SQS/L and LI 250A, Walz). Light profiles within the sediment were measured using a self-made fiber optic scalar irradiance microsensor, consisting of a light guiding fiber with a polystyrene sphere (diameter ~200 µm) with suspended titanium dioxide particles for light scattering at its end (Lassen et al. 1992b). Data acquisition to a PC was done with a 12 bit A/D converter (DAQPad 6020E, National Instruments). The light microsensor was calibrated against the above-mentioned quantum sensor. For this purpose, the downward scalar irradiance of a white power LED at different operating currents was measured with the factory-calibrated quantum sensor and the self-made microsensor, both mounted above a black anodized aluminum tube as light trap (data not shown). For light intensity profiles, the microsensor was mounted in a micromanipulator, fixed to a motorized stage (VT-80, Micos) to allow for automated profiling. Since the light acceptance of the microsensor is lowest in the direction of the fiber, profiling (step width 100 µm) was done in an angle of 60° to the sediment surface.

To calibrate the light measurements performed with the HiPO, a light-field image of the sandy sediment was averaged over all columns. Two points of the resulting profile were related to light measurements, made at the same depth with the light microsensor. All measured pixel intensities were scaled accordingly, assuming a linear relationship. Since the camera was equipped with a long-pass filter, only red light was imaged.

The light acceptance of the setup depends on the numerical aperture of the fibers and the light-scattering properties of the sensing chemistry. We measured the light acceptance at different angles, ranging from 20° to 160°. A laser line was projected from different angles onto the sensing layer under artificial seawater (salt content 35‰). The captured light was imaged with the CCD-camera from the other side. After averaging over all lines, the total peak area was integrated to correct for the wider peaks at more acute angles. Values were normalized to the measurement at 90°.

Modeling of oxygen diffusion within sensing chemistry—Diffusion of oxygen within sensing chemistry leads to reduced measurements of the actual gradients and sets an upper boundary for the differentiation of adjacent features in the oxygen concentration field. To quantify this effect, finite-element numerical modeling of oxygen diffusion within a planar optode sensing layer was carried out, using the software COMSOL (COMSOL AB, Stockholm). The sensing chemistry was modeled as a 20-µm thick layer of polystyrene ($D[O_2] = 4 \times 10^{-11}$ m^2 s^{-1}, Poulsen and Ogilby 2000). Initially completely anoxic, half was modeled to be exposed to a step change to 100% air saturation whereas all other boundaries were set to isolation conditions. The transient solution of the diffusion equation for two dimensions (Crank 1979) was solved on a domain that represented a cross-section through the sensing layer. To calculate the response of the sensing chemistry, we assumed that the fluorescence signal for each point on the HiPO surface is the sum of calculated responses throughout the thickness of the sensing layer.

Combined measurements in sandy sediments—The HiPO was applied for combined oxygen and light-field sensing on sandy sediment from the subtidal zone of the island Sylt. The sediment was sieved with a 500 µm mesh to exclude macrofauna and pre-incubated in the measurement setup for 1 week with a light–dark cycle of 12 h at 100 µmol photons m^{-2} s^{-1}. The apparent sediment diffusion coefficient D_s = 8.6e-10 $m^2 s^{-1}$ was estimated from the oxygen diffusion coefficient in seawater with a salinity of 35 at 20°C (D_0 = 1.99e-9 m^2 s^{-1}, calculated

after Boudreau (1997), and a sediment porosity of 0.43 as determined by 48 h drying at 60°C, using Archie's Law (e.g., Berner 1980). Benthic photosynthesis was measured at three different incident irradiances (I_d), identified throughout the manuscript as I_d(A) = 280, I_d(B) = 100, and I_d(C) = 40 µmol photons m^{-2} s^{-1}. Each illumination period lasted for 3 h, followed by 3 h darkness (Fig. 3). Images for scalar irradiance estimations were taken for the three light conditions at the beginning and at the end of the experiment.

Calculation of respiration and photosynthesis rates—The distribution of oxygen concentration within sediments is governed by production, respiration, chemical oxidation, and diffusion. The reaction-diffusion equation describing these processes for two dimensions reads as:

$$\frac{\partial C}{\partial t} = -\phi D_s \left(\frac{\partial^2 C}{\partial x^2} + \frac{\partial^2 C}{\partial z^2} \right) + (P - R) \qquad (1)$$

where C is oxygen concentration, x is the horizontal dimension, z is sediment depth, and t the time. P and R are time- and space-dependent oxygen production and uptake terms, respectively, and D_s is the sediment diffusion coefficient. Neglecting the third dimension (horizontal and perpendicular to the HiPO) is necessary, because only 2D information about the oxygen concentration is available. After a minimum of 2 h with constant irradiance, a steady-state situation established, where $\partial C/\partial t = 0$. For any given point within the sediment, the loss of oxygen by diffusion, respiration, and chemical oxidation is balanced by production of oxygenic photosynthesis. After darkening, photosynthesis stops instantaneously resulting in a non-steady-state situation.

Because the reaction time of the optode was not sufficient to carry out conventional light–dark shift measurements (taking only the decline in oxygen concentration within the first few seconds after darkening into account), we adapted the method developed by Epping et al. (1999) for 2D, using transient oxygen images rather than oxygen profiles.

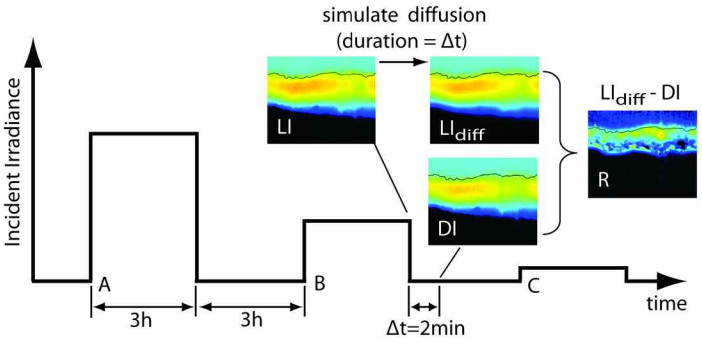

Fig. 3. Calculation of 2-D respiration rates from transient oxygen images after changes in incident irradiance. A light image (LI) is taken at steady-state and the effect of 2 min of diffusion alone is calculated (LI_{diff}). Two minutes after the light was switched off, the dark image (DI) is recorded. The difference between LI_{diff} and DI is an estimate of the spatial distribution of respiration rates within the sediment (R). The calculation of net photosynthesis was carried out in a similar way but after the onset of illumination. The letters A, B, and C represent the three different light conditions used subsequently in this study. The duration of each light and dark period was 3 h.

Therefore, the numerically calculated effect of oxygen diffusion is compared with the measured effect of diffusion plus oxygen consumption. To calculate oxygen consumption rates, the following procedure was used: Oxygen images were taken during illumination at steady-state (light image; LI) and 2 min after the light was switched off (dark image; DI, Fig. 3). We then assumed that after the light was switched off, the two remaining processes affecting the oxygen distribution are diffusion and O_2 consumption. To determine the sole effect of diffusion, the LI was blurred by filtering (convoluting) it with a Gaussian kernel (Koenderink 1984; standard deviation: 45 pixels). This operation simulates 120 s of diffusion, assuming a sediment diffusion coefficient of D_s = 8.6e-10 m^2s^{-1} with the LI oxygen concentrations as initial condition and zero-flux boundary conditions. This numerical solution of the diffusion equation is commonly used in image analysis (Koenderink 1984; Cai 1988). To ensure the applicability and precision of this method for our application, it was tested against an explicit numerical diffusion scheme, resulting in differences < 2% (Wolf-Gladrow pers. comm.). The calculated image (LI_{diff}) was then compared with measured DI where diffusion and respiration influenced the oxygen distribution. The pixel-by-pixel difference between these two images represents an estimation of the spatial distribution of respiration (Fig. 3). A similar approach was used to estimate primary production. Here, the first image was taken in the dark after steady-state was reached. A diffusion step was calculated and the obtained image was compared with a measured image taken after 2 min illumination. Note that the resulting photosynthetic rate represents the net photosynthesis, e.g., production minus respiration ([$P - R$] in Eq. 1). The relatively long-time step of 2 min was necessary because of the low production and respiration rates of the studied sediment.

Calculating profiles and integrating respiration and production rates—Quantitative comparison of scalar irradiance, respiration rates, and photosynthesis was done by averaging 2D data to one-dimensional (1D) profiles, represented by every column of the respective images, taking the different positions of the sediment surface into account. Diffusive exchange of oxygen (DOE) across the sediment-water interface (z = 0) was calculated from the mean oxygen profiles using Fick's first law of diffusion

$$\mathrm{DOE} = -D_0 \left. \frac{\partial C}{\partial z} \right|_{z=0} \qquad (2)$$

with the molecular diffusion coefficient of oxygen in seawater D_0 = 1.99e-9 m^2 s^{-1}.

Local rates of respiration and net primary production were integrated over depth (z) and averaged over all columns of the

image, resulting in areal oxygen fluxes:

$$J_R = \frac{\Delta z}{n} \sum_{n=1}^{n_{max}} \sum_{z=0}^{z_{max}} R_{n,z} \quad and \quad J_P = \frac{\Delta z}{n} \sum_{n=1}^{n_{max}} \sum_{z=0}^{z_{max}} P_{n,z} \qquad (3)$$

with F_R and F_{PP} being the fluxes across the sediment-water interface, Δz the pixel size (Δz = 10.1 µm), n the numbers of columns (n_{max} = 1280), and $R_{n,z}$ and $P_{n,z}$ the respiration and production rates at column n and depth z as calculated above.

The mean vertical light attenuation coefficient K was calculated from the average scalar irradiance profiles $I(z)$ below 0.5 mm by fitting an exponential function to the profiles (Kühl et al. 1994): $I(z) = \alpha e^{-Kz}$ with α as arbitrary fit parameter.

Local photosynthesis/irradiance relationship and photosynthetic efficiency—The availability of scalar irradiance and photosynthesis distributions allowed calculating local photosynthesis/irradiance relationships for each of the three light conditions. These curves differ from conventional P-I curves, since they consider the local effect of scalar irradiance on net photosynthesis rather than providing the averaged budget for the sediment (Dodds et. al. (1999) for the 1D case). The curves were constructed by binning the scalar irradiances with a bin-width of 10 µmol photons m^{-2} s^{-1}. The corresponding photosynthesis rates of all pixels that fell into one bin were averaged and plotted against the mean irradiance of the respective bin.

To assess the relative efficiency of light use by the phototrophic community and its variation with sediment depth, the quotient of photosynthetic rate and scalar irradiance was calculated, resulting in photosynthetic efficiencies in units of [mmol O_2 mol photons^{-1} mm^{-1}] (Lassen et al. 1992a).

Assessment and discussion

Optical cross-talk effect—Light travels within the support foil and the window of conventional planar optode setups by reflection on the surfaces (Fig. 1a). Part of this light is decoupled on other sites of the foil and contributes to the fluorescence, originating from these spots. The overall fluorescence intensity is therefore altered, as well as the fluorescence lifetime (τ) (Franke 2005). Because the fluorescence is quenched by oxygen, light emission is stronger in anoxic regions than in oxic regions. The anoxic parts of the sediment thus influence the measurements in oxic areas stronger than the reverse. Overall, this artifact results in smeared images and flattened gradients. This decreases the significance of calculations of fluxes and respiration rates, especially if the heterogeneity on small scales is high.

The HiPO was compared against a conventional PO setup to test if this optical cross-talk could be reduced. A small flume comprising HiPO and conventional PO was half filled with anoxic distilled water. The overlying gas phase was initially nitrogen and then rapidly changed to air, leading to highly reproducible sharp oxygen gradients across the water–air interface. In contrast to the conventional PO, no erroneously low oxygen concentration was measured above the interface

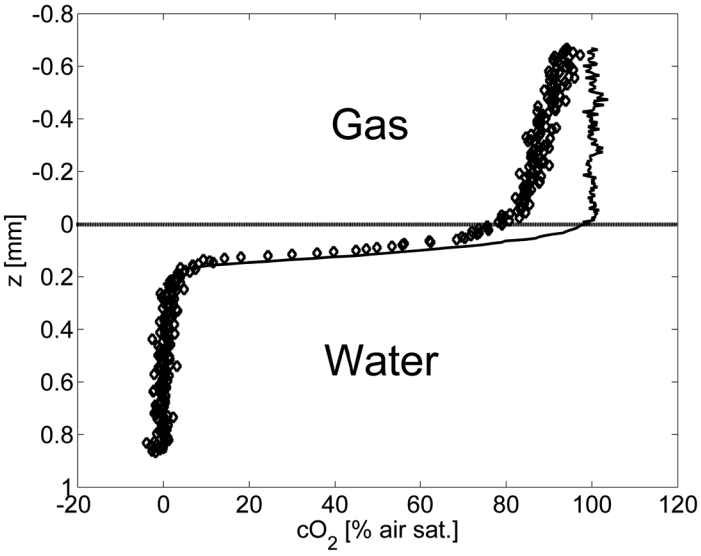

Fig. 4. Extracted vertical profiles of oxygen concentration after changing the gas phase over anoxic water from nitrogen to air, measured with the HiPO (solid line) and a conventional PO (open symbols). For practical purposes, data from the conventional optode can be partly corrected with a priori knowledge about the oxygen concentration in the water column.

with the HiPO (Fig. 4), indicating an effective suppression of the cross-talk effect. Hence, the recorded gradient appeared much steeper with the HiPO, as it was with the conventional setup. For practical purposes, cross-talk artifacts at the sediment-water interface can be taken into account, using the a priori knowledge about the oxygen concentration in the water column. Within the sediment, however, such a correction is not possible.

The magnitude of optical cross-talk effects in conventional PO assemblies depends on a multitude of factors, such as wall thickness and material, thickness of the support foil, content of scattering particles within the sensing layer, and distribution of sediment oxygen concentration, to name only a few (Glud 2008). It is beyond the scope of this study to determine the relative influence of all these factors, and it is therefore not possible to precisely quantify the improvement gained by using the HiPO.

Spatial and temporal resolution of oxygen measurements—The theoretically achievable spatial resolution of the HiPO system is limited by the optical performance of the setup and the blurring of the signal due to oxygen diffusion in the sensing chemistry (Kühl et al. 2007). The temporal resolution of all PO setups is regulated by the equilibration time of the sensing chemistry. To estimate the magnitude of both effects for the HiPO setup, a numerical diffusion model was set up, using finite element modeling as described in the methods section. This model allowed calculating the transient and steady-state oxygen fields within a cross-section of the sensing layer, assuming a step change on the surface of the (polystyrene) sensing layer (Fig. 5A). Profiles of the response of the sensing

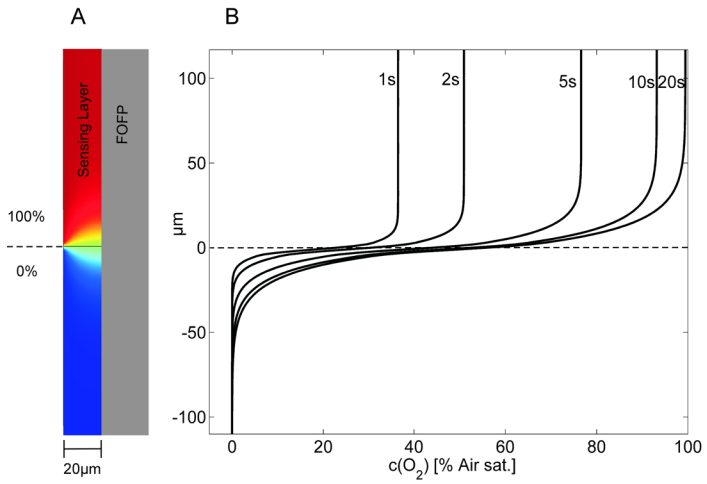

Fig. 5. (a) Modeled steady-state oxygen concentration within a cross section of a 20-µm thick sensing layer, exposed to a step change in oxygen concentration at $y = 0$ µm. The FOFP is impermeable for oxygen. *See* Fig. 4 for the color scale; values in percentage air saturation. (b) Modeled temporal and spatial response of the sensing layer to a step change in oxygen concentration. Initially, the foil was modeled to be completely anoxic. At $t = 0$ second, the upper half ($y > 0$ µm) was exposed to 100% air saturation.

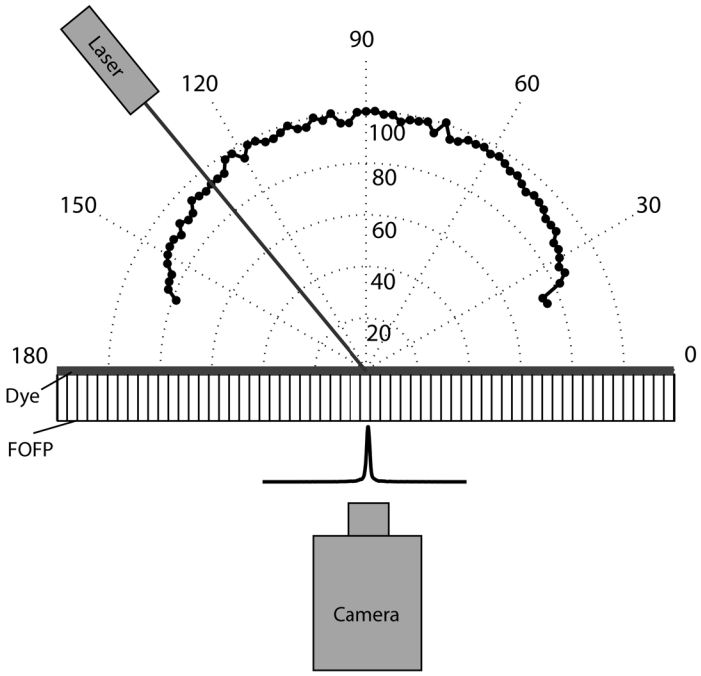

Fig. 6. Light-acceptance angle of the FOFP with scattering sensing layer. A laser line was projected onto the surface under seawater at different angles and the captured light was imaged with a CCD camera. Measured peak areas are given, normalized to the 90° value.

layer (Fig. 5B) were obtained by averaging over all columns of the calculated oxygen field within the sensing layer of Fig. 5A. This model can also be used to estimate the temporal response of the sensor after a change in oxygen concentration (Fig. 5B). If the sensor is initially oxygen-free and then the oxygen level is raised to 100% for half of the sensor surface, oxygen diffuses into the sensing chemistry changing the fluorescence properties in this area. After 1 s, the signal only reached 36% of the final concentration. A typical 90% response is reached between 5 and 10 s for a 20-µm thick sensing layer. After ~20 s, steady-state is reached. The sharp boundary between the oxic and anoxic zone is then smeared and extended over about 100 µm (Fig. 5). The response of the sensing layer to a step change in concentration represents the highest gradient that can be resolved by the system. Thus, it provides the theoretical limit of resolution given by diffusion in the sensing layer. For all practical concerns, the difference between the "real" oxygen concentration and the one measured by the PO setups will be smaller than in this extreme example.

Model runs assuming thinner sensing layers showed a linear relationship between layer thickness and spatial resolution (results not presented). A 2-µm thick layer therefore exhibits a resolution limit of about 10 µm. Because the change of layer thickness essentially affects only the scale of the model, this linearity is obvious. The resolution limit of planar optodes due to diffusion is therefore in the order of 5 times the thickness of the sensing layer, assuming polystyrene as matrix polymer. Thinner layers, however, demand for stronger excitation light sources and/or more sensitive cameras. Layers of 10-20 µm were found to be a good compromise for our setup. Thinner layers are possible, if a stronger excitation light source is used or the imaged area is reduced (Kühl et al. 2007). Other possibilities include the use of a more sensitive camera and the potential addition of light-harvesting molecules to the matrix (Mayr et al. 2009). Using polymers with a higher molecular diffusion coefficient for oxygen would result in faster responding optodes, but lower spatial resolution.

2D light-field measurements—The penetration of light into sediments is not uniform due to scattering and refraction at sediment grains, worm borrows, and gas bubbles, resulting in a patchy distribution of irradiance (Lassen et al. 1992a; Kühl et al. 1994). Scalar irradiance is defined as the integrated light from all directions. Sensors for scalar irradiance therefore need to have a spherical acceptance characteristic. Very close to a wall, however, light can only originate from one side, and hemispherical acceptance is sufficient. Projections of a laser line from different angles were performed to assess the acceptance angle of the HiPO (Fig. 6). Between 60° and 120° incident light was transported equally well, while in the range of 40°-60°, capture efficiency drops to 90%. Below 20°, a strong drop in light acceptance was observed (Fig. 6). This almost hemispherical acceptance characteristic of the HiPO allows the use of light-intensity images taken through the HiPO as a measure for scalar irradiances. Note that the spatial heterogeneity of scalar irradiances close to walls (like the HiPO) is likely to be higher than in unconstrained sediments. Especially in the top layers of the sediment where heterogeneities are most pronounced (Lassen et al. 1992a), the HiPO tends to overestimate spatial variability of the irradiance. Assuming a 20-µm thick

sensing layer and a light acceptance angle of 130°, a theoretical resolution of ~120 µm can be expected. This is in the same order of magnitude as the resolution of typical scalar irradiance microsensors (Lassen et al. 1992b).

Light-field images were measured in sandy sediments and compared with light profiles obtained with microsensors for scalar irradiance (Lassen et al. 1992b). The images exhibit a high spatial variability, both horizontally and vertically. Light profiles were extracted by averaging intensities over columns of a 100-µm wide stripe (Fig. 7). Profiles differ considerably from each other due to different scattering, resulting in hot spots of high-light intensities in otherwise darker sediments. Highest light intensities are not always directly above the sediment surface, and the light intensity does not decrease steadily below the surface. However, the overall light penetration depth (defined as the depth, where scalar irradiance drops below 1 µmol photons m^{-2} s^{-1}) is similar in all extracted profiles (Fig. 7).

Mean profiles were extracted at three different incident irradiances by averaging over all columns of the intensity images and were compared with scalar irradiance microsensor measurements (Fig. 8). Strongest differences were observed above the sediment surface. Here, the HiPO provides up to 10% lower values than the microsensor. The reason might be that most of the light reflected at the sediment surface is traveling upwards. For spherical microsensors profiling from the top, this is the preferred acceptance direction, while the HiPOs fibers are directed perpendicular. However, the microsensor readings are within the double standard deviation of the averaged columns' readings, indicating an overall agreement between both methods (Fig. 8, left). The better accordance of the two methods deeper within the sediment is related to the fact that the light field tends to approach isotropic radiance distribution with depth (Kühl et al. 1994). Comparisons at different light levels (Fig. 8, right) reveal the same profile pattern indicating that the HiPO can be calibrated against a scalar irradiance microsensor.

The most important difference between the two methods is the spectral response. The light microsensor can be used to assess spectral compositions of scalar irradiance or total photosynthetically active radiation (PAR) by using a spectrometer as detector (Kühl and Jørgensen 1994). The spectral properties of the light-field measurements with the HiPO are dependent on the spectral response of the CCD camera, the transmission characteristics of the FOFP with the fluorophore coating and the emission filter for oxygen sensing. The spectral response of the camera was nearly linear between 350 and 550 nm wavelength, therefore it is, in principal, suitable to measure PAR. However, the emission filter was a long-pass filter with a cut-off wavelength of ~580 nm, allowing only red light to pass through. If the spectral composition of the down-welling light does not change substantially within the sediment, the calibration against the PAR sensor in the overlying water is still valid for deeper layers. This assumption depends on the concentration and distribution of pigments within the sediment. It is known, that highly structured phototrophic communities absorb different wavelengths at different depth (e.g., Ploug et al. 1993). This effect is less pronounced in sandy sediments due to the generally less structured community.

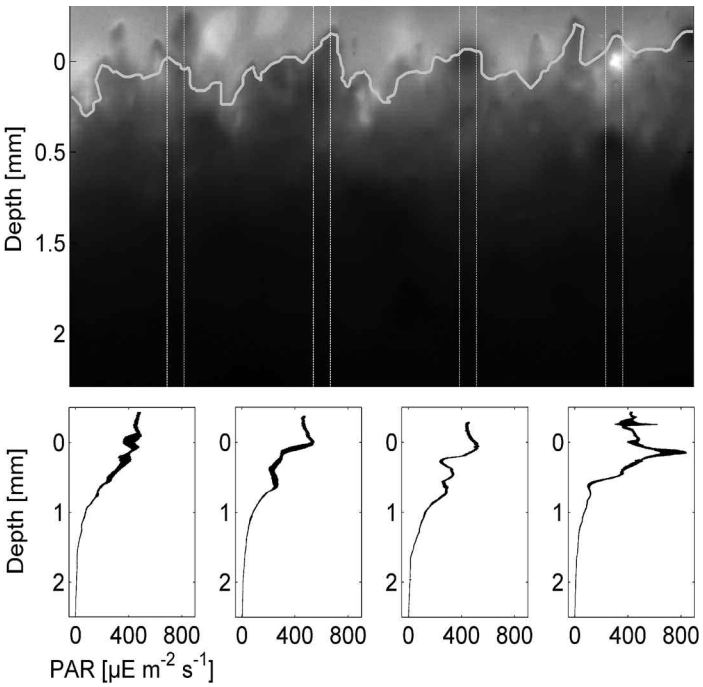

Fig. 7. (Top) Light intensity image of a sandy sediment, taken through the HiPO. The sediment was illuminated from above with white light. (Bottom) Four light profiles, each extracted from a 100-µm wide area of the image by averaging along the *x* axis. The line width in horizontal direction indicates the standard deviation of the measured irradiance at each pixel.

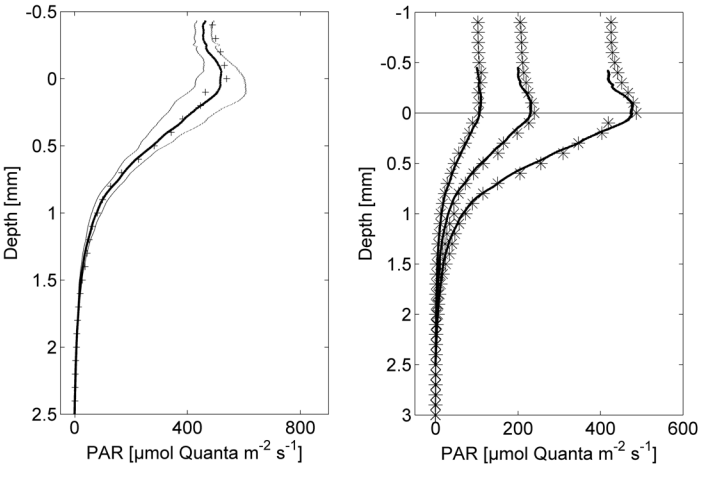

Fig. 8. (Left panel) Mean light profile, extracted from the light intensity image in Fig. 7 by averaging over all columns (thick line), standard deviation of the intensities (thin lines) and light profile, measured with a light microsensor (plus symbols). (Right panel) Comparison of light profiles measured with a light microsensor and profiles obtained by averaging over all columns of an intensity image at 100, 200, and 410 µmol photons m^{-2} s^{-1}, respectively.

Oxygen dynamics in sandy sediments—Small-scale oxygen distributions and dynamics and their linkage to the light field have been studied extensively on microbial mats (e.g., Lassen et al. 1992a; Epping et al. 1999; Glud et al. 1999; Bachar et al. 2008), but less work has been done on sandy sediments without dense mat formation. Therefore, we applied the HiPO to phototrophic sandy sediments and measured oxygen production and respiration together with the light field as major driving force (Fig. 9). The sediment was inhabited (among others) by diatoms and cyanobacteria, exhibiting considerable photosynthesis during illumination.

Light field within the sandy sediment—The different incident light intensities, measured as downwelling irradiances above the sediment surface are indicated in Figs. 9–11 by the letters: A, B, and/or C (40, 100, and 280 µmol photons m^{-2} s^{-2}, respectively). The light field within the sediment (Fig. 9, column 1) was highly inhomogeneous at submillimeter scale, most likely due to reflections and refractions by sediment grains. This effect was most pronounced close to the sediment surface, as reported earlier (Kühl et al. 1994). Highest local light intensities were detected ~100–200 µm below the sediment surface. Here, the scalar irradiance exceeded 200% of the surface downwelling irradiance at some spots. The average light penetration depth (defined as the depth, where scalar irradiance drops below 1 µmol photons $m^{-2}s^{-1}$) was 5, 4.2, and 3.3 mm, at the three light conditions respectively (Fig. 10, Table 1). The three mean scalar irradiance profiles showed the same exponential decrease with depth

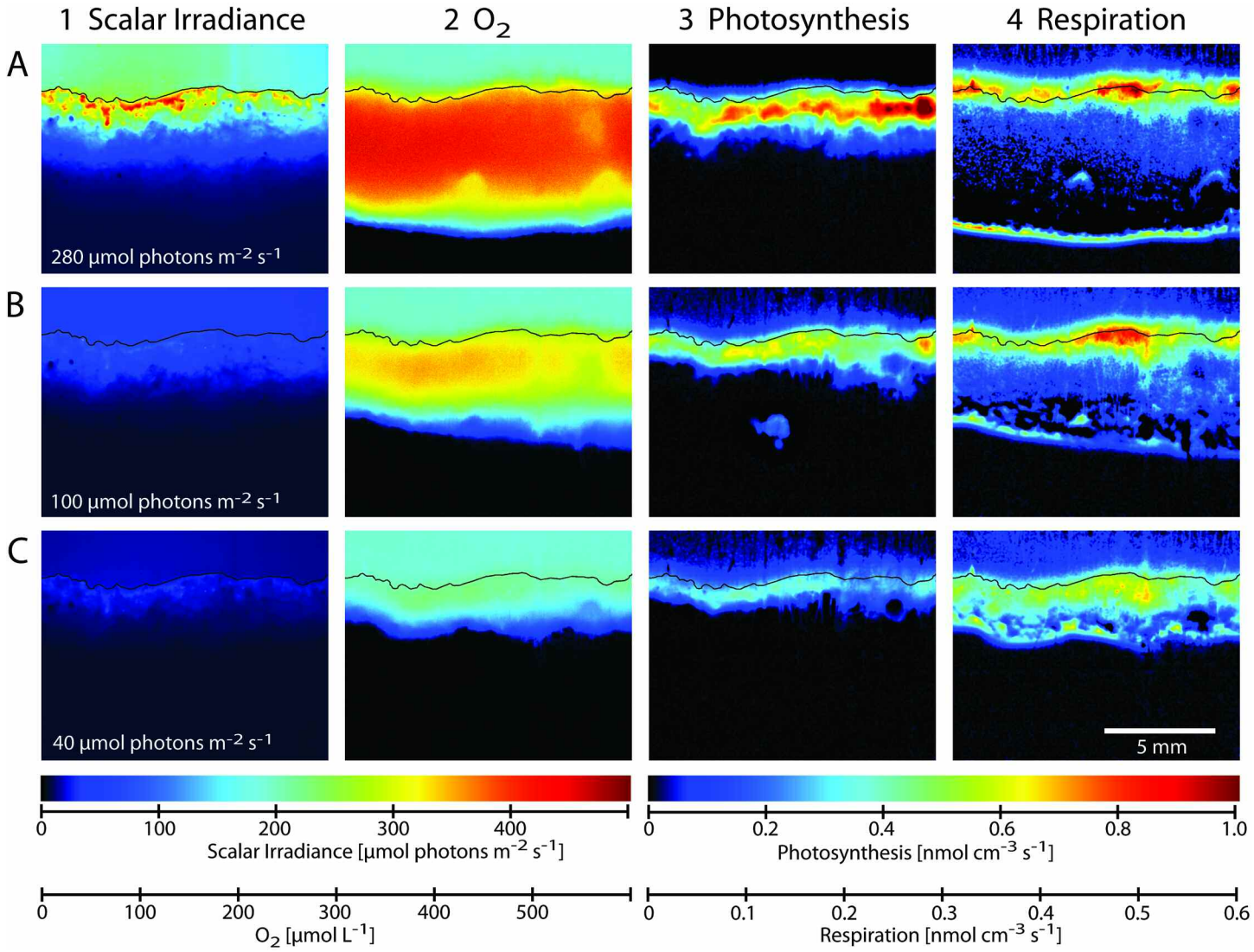

Fig. 9. Images of light (1), oxygen (2), net photosynthesis (3), and respiration (4) at three different light conditions (A, B, C) in phototrophic sandy sediment after steady-state was reached. The black line indicates the sediment surface. Pixel size in theses images was 10.1 µm. The productive spot visible in the middle of the imaged area in B3 was related to a gas bubble formed as a result of the oxygen supersaturation during high light condition, supplying oxygen to the surrounding sediment.

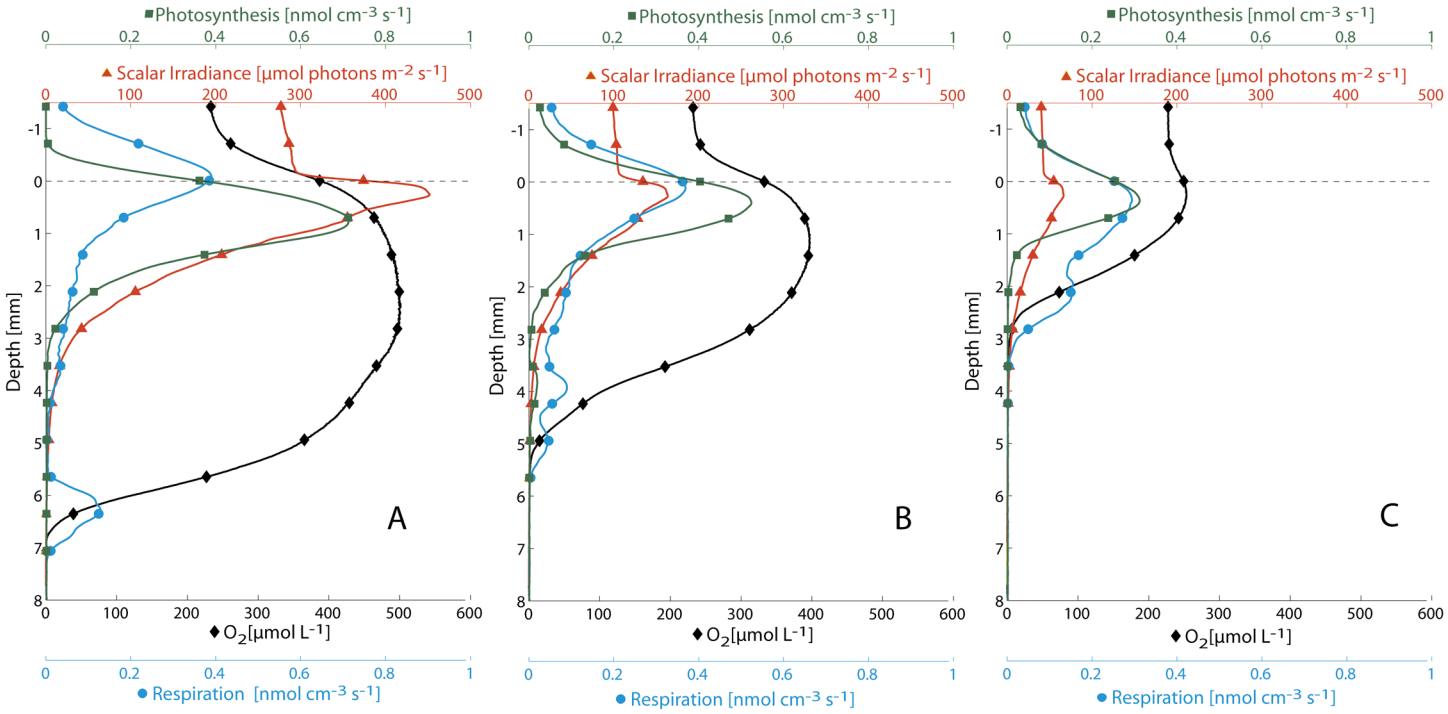

Fig. 10. Profiles of scalar irradiance, oxygen concentration, respiration rate, and photosynthesis rate at three different steady-state situations (A, B, C) with different illuminations. The profiles were obtained by averaging over the columns of Fig. 9, taking the position of the sediment surface into account. Symbols represent every 70th data point.

(Table 1, $R^2 > 0.99$), leading to a mean vertical light attenuation coefficient K of 0.85 mm^{-1}. Kühl et al. (1994) found a twice as high attenuation coefficient for wet quartz sand with particle sizes of 125–250 µm (1.65 mm^{-1}) and a four times higher attenuation coefficient for a coastal sediment with particle sizes of 63–250 µm. The lower light attenuation in our study can be explained by larger particles sizes of up to 450 µm and the low density of light-absorbing photopigments (*see* below).

Oxygen concentration field—The oxygen concentration field changed clearly within minutes upon changes in light conditions. However, transition times of more than 2 h after each change in illumination were needed to establish new steady-state situations. Similar transition times were found by Fenchel and Glud (2000) for a shallow water sediment. At high incident light [I_d(A)], the first 5 mm of the sediment were oxygen super-saturated with concentrations up to 500 µmol L^{-1}; the mean oxygen penetration depth was about 6.8 mm, and there was a net flux of oxygen (36 mmol m^{-2} d^{-1}) into the overlying water (Fig. 10 and Table 1). The oxygen concentration distribution did not exhibit strong spatial heterogeneities on scales below 1 mm (Fig. 9, A2). After the light was switched off, oxygen concentrations immediately decreased, especially close to the sediment surface. However, the formation of three oxygen bubbles in the imaged area with diameters between 0.7 and 2 mm led to zones of supersaturation that persisted for more than 1 h (data not shown). At I_d(B), the mean oxygen penetration depth reduced to 5.2 mm (Fig. 10B). There was a considerable difference in OPD within the averaged area, ranging from 3.9 to 5.6 mm (Fig. 9, B2). The oxic-anoxic interface was characterized by smaller gradients, also with strong horizontal differences; the super-saturated zone reduced to a mean of 3.5 mm sediment depth (Fig. 9) and showed stronger heterogeneities compared with those at high-light intensities (Fig. 9, B2). At I_d(C), still slight super-saturation occurred and photosynthesis exceeded respiration, leading to a net flux of 7 mmol m^{-2} d^{-1} O_2 out of the sediment (Table 1). The mean oxygen penetration depth reduced to 3.1 mm and the oxic-anoxic transition zone was even less straight compared with medium light conditions (Fig. 9, C2). During all three steady-state darkness situations between the illuminations, the mean oxygen penetration depth reduced to 1.7 mm (Table 1).

Local net photosynthesis rates—Photosynthesis (Fig. 9, column 3) was calculated from subsequent images immediately before and directly after the onset of illumination. This procedure results in estimations of local net photosynthesis rates. At I_d(A), highest rates of net photosynthesis were observed on average 900 µm below the sediment surface (Fig. 10 A) and appeared very patchy (Fig. 9, A3). The peak values of more than 1 nmol O_2 cm^{-3} s^{-1} were not located at the spots of highest light intensity within the sediment. Photo adaptation could explain this effect, as well as migration due to light stress (Macintyre and Cullen 1995; Underwood et al. 2005). The entire productive zone was about 3.5 mm thick and

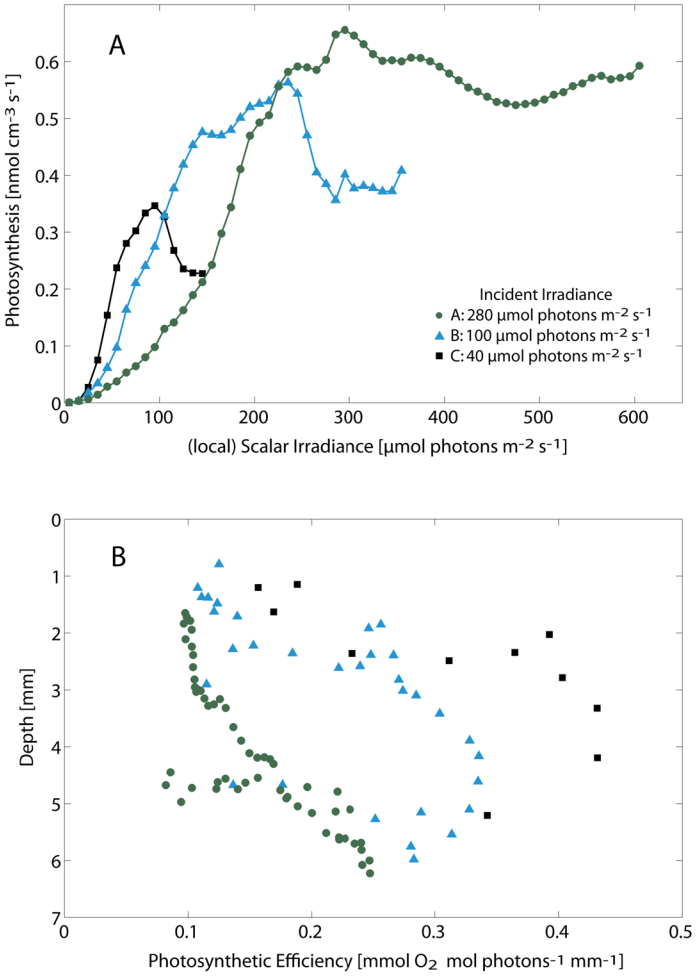

Fig. 11. (A) Average local photosynthesis plotted against average local scalar irradiance (Fig. 9, column 1 and column 3). The three curves represent the three different illuminations (A, B, C) as in Figs. 9 and 10. (B) Photosynthetic efficiency at the three light conditions, calculated as the local photosynthesis divided by the local scalar irradiance and plotted against sediment depth.

almost identical to the area, in which light intensities were > 30 µmol photons m^{-2} s^{-1} (Fig. 10A). At medium light conditions [I_d(B)], the overall thickness of the productive zone was only slightly reduced (~3 mm), but the peak values of photosynthesis diminished and the heterogeneity in production was less pronounced. Highest production was now close to areas with highest light intensities but the average position of peak photosynthesis was still below the position of peak scalar irradiance (Fig. 11B). At I_d(C), the zone of primary production was limited to a thickness of 1 mm. A spatial coincidence of peak scalar irradiance and photosynthesis rates was found for this lowest incident irradiance (Figs. 9, C1, and 9, C3; Fig. 10C).

Correlation of local net photosynthesis and light availability—The relationship between local net photosynthesis and scalar irradiance at the respective positions within the sediment was used to construct curves of mean local photosynthesis versus scalar irradiance (Fig. 11A). A comparable approach in 1D was taken by Dodds (1992) and Dodds et al. (1999). However, they used the light–dark shift method and reported local gross photosynthesis-irradiance curves for different depth intervals, whereas we provide curves of net photosynthesis versus irradiance, averaged over all measurements at one incident irradiance. The curves in Fig. 10A differ from conventional P-I curves because they do not represent the average response of the whole sediment community to changing incident light intensities but the mean local response to the resulting scalar irradiance within the sediment. All three curves show the same general pattern of increasing photosynthesis with increasing irradiance, until a maximum is reached (Fig. 10A). At higher irradiances, the photosynthetic activity decreases again, most likely due to photoinhibition (e.g., Serôdio et al. (2005) and references therein). Therefore, curves calculated for the three different I_d exhibit maximum photosynthesis rates at different light intensities. While at I_d(A), the highest photosynthetic rates were observed at around 300 µmol photons m^{-2} s^{-1}, this value was reduced to 230 and 100 µmol photons m^{-2} s^{-1} for I_d(B) and I_d(C), respectively (Fig. 11A). Since the same scalar irradiance is found in different depth within the sediment at different incident light conditions, it is likely that the responses reflect a stratified community. Adaption to the incident irradiance on single-cell level even in time scales of minutes (Serôdio et al. 2005), as well as migratory behavior of algal cells (Barranguet et al. 1998; Saburova and Polikarpov 2003) and cyanobacteria (Castenholz et al. 1991) are also likely.

Photosynthetic efficiency—The efficiency of light use by the phototrophic community changes with depth in the sediment as well as with incident light intensity (Fig. 11B). A general trend of increasing photosynthetic efficiency with depth can be seen. At I_d(A), no maximum is reached while at I_d(B) and I_d(C) maximum values are located in 4.5 and 3.5 millimeter sediment depth, respectively. As a consequence of light adaptation, the maximum efficiency at the lowest incident irradiance (0.42 mmol O_2 mol photons^{-1} mm^{-1}) is higher than at medium irradiance (0.32 mmol O_2 mol photons^{-1} mm^{-1}). Lowest efficiencies are found for I_d(A). The net photosynthetic efficiency depends on the prevalent respiration rate and the amount of photopigments present. It also depends on the efficiency with which the captured light is used for photosynthesis (Lassen et al. 1992a). The latter is partly dependent on irradiance and decreases as the intensity exceeds the light saturation of the population. The differences of photosynthetic efficiencies between the three different incident light intensities can therefore be explained by photo-acclimation, changing the efficiency of single cells (Serôdio et al. 2005) and migration of phototrophic organisms (e.g., Perkins et al. 2001; Underwood et al. 2005), changing the pigment concentration in a given sediment horizon. Lassen et al. (1992a) found comparably shaped profiles of photosynthetic efficiency with depth and a comparable influence of different incident light intensities for microbial mats. However, their reported efficiencies exceed the values presented here by 2 to 3 orders of

Table 1. Downwelling irradiance I_d, vertical light attenuation coefficient K, oxygen penetration depth z_{ox}, and oxygen budget for sandy sediment at three different illuminations. Oxygen penetration depth, light attenuation coefficient, and DOE have been calculated from the mean oxygen profiles (Fig. 9). Integrated rates of respiration (J_R) and net photosynthesis (J_P) were calculated from data presented in Fig. 9, columns 3 and 4. A, B, and C correspond to the respective panels in Figs. 9–11. Values in the last line were calculated from an oxygen image at steady-state situation during the dark (image not shown). Negative values imply fluxes out of the sediment.

Panel	I_d (µmol photons m^{-2} s^{-1})	K (mm^{-1})	z_{ox} (mm)	J_R (mmol m^{-2} d^{-1})	J_P (mmol m^{-2} d^{-1})	DOE (mmol m^{-2} d^{-1})	J_P + DOE (mmol m^{-2} d^{-1})
A	280	0.85	6.8	–47	89	–36	53
B	100	0.86	5.2	–53	54	–29	25
C	40	0.84	3.1	–49	24	–7	17
—	0	—	1.7	—	—	22	—

magnitude. The most likely reason is the much higher pigment density in microbial mats compared with the sandy sediment in our study. The low light attenuation coefficient of our sediment (*see* above) underlines this assumption.

Oxygen exchange rates and O_2 budget—The distribution of oxygen exchange rates within the sediment exhibited two conspicuous zones of high consumption at all three light conditions (Fig. 9, column 4). One was located directly at the oxic-anoxic interface. It can be explained by chemical oxidation of reduced compounds that are formed during anaerobic metabolic activities, diffusing upwards (e.g., Canfield et al. 1993). Additionally, some microorganisms (e.g., some species of sulfate reducing bacteria) live preferentially in this transition zone and respire oxygen at high rates (Cypionka 2000). This zone was most obvious at I_d(A), where it was located deepest within the sediment and had a thickness of < 1mm (Fig. 9, A4). Here, reoxidation processes are likely to be more relevant than further upwards due to the higher relative importance of anaerobic processes deeper in the sediment. Such narrow zones of very high oxygen uptake directly at the oxic-anoxic interface have been reported before (e.g., Revsbech et al. (1986). The second zone of high oxygen uptake was located close to the sediment surface. Here, again, two mechanisms play a role; the density of respiring organisms and the accumulation of labile organic matter are likely to be highest close to the sediment surface. Additionally, photoexudates, excreted by phototrophic organisms, might have fueled oxic respiration (Bateson and Ward 1988). Because of the net oxygen production some of the oxygen is also removed by diffusion into the well-mixed overlying water column. However, the modeling of diffusion did not account for the enhanced eddy diffusivity in the water column above the sediment surface. Thus, calculated rates of respiration above the surface should be taken with caution.

The integrated dark respiration rates in the order of ~20 mmol m^{-2} d^{-1} (Table 1) are in the range of values found for coastal sandy sediments (Middelburg et al. 2005). The average O_2 consumption is stimulated to ~50 mmol m^{-2} d^{-1} during illumination. Similar increases in light-respiration have previously been reported (e.g., Epping and Jørgensen 1996; Fenchel and Glud 2000).

Integrated rates of oxygen consumption and production are used to compile oxygen budgets for the different light conditions. The diffusive oxygen flux across the sediment/water interface (DOE) under illuminated conditions is governed by the integrated rates of net photosynthesis (J_P), comprising gross photosynthesis plus respiration. These two parameters should therefore match. However, J_P shows a higher efflux of oxygen from the sediment than the average DOE at all three light conditions, while the differences decreased with decreasing irradiance (Table 1). These discrepancies between DOE and J_P might indicate different respiration rates in the light and in the dark. The net photosynthesis rates (J_P) were obtained directly after the onset of illumination; they thus include a sediment respiration close to the dark respiration, while the DOE was determined 3 h after the onset of illumination and represent the higher light respiration, where photoexudates and the increased area of the oxic zone resulted in enhanced oxygen uptake (Epping and Jørgensen 1996). It is also likely that the mean DOE was underestimated by the averaging procedure, used to obtain a single oxygen profile from an oxygen image, since small inaccuracies in the position of the sediment surface lead to a smeared gradient in the average profile. Additionally, the formation of gas bubbles may lead to underestimations of DOE (Epping and Jørgensen 1996), and the PO might interfere with the diffusive boundary layer (DBL) (Glud 2008).

A light-enhanced respiration, however, is not reflected in the integrated respiration rates (J_R, Table 1). The assumption of the same molecular diffusion coefficient in the water column as in the sediment rather than eddy diffusion bias the respiration rates calculated for areas closely below the sediment surface. Changes in respiration rates during the time step of 2 min before the dark respiration image was taken are possible. More sophisticated modeling of the diffusion step and additional light–dark shift measurements with microsensors could be performed to clarify these uncertainties.

Comments and recommendations

The novel planar optode imaging setup allows gaining spatially resolved insights into oxygen dynamics in phototrophic sediments and microbial mats at high spatial resolution together with local estimations of scalar irradiance. This facil-

itates studies concerning the functioning of phototrophic microbial communities in detail, together with the local light field as the most important driving force. The HiPO and the proposed calculation scheme enable the determination of spatial correlations of photosynthesis and respiration rates with the scalar irradiance distribution. New insights into the coupling between autotrophic and heterotrophic communities and their spatial organization can be gained. It provides higher certainty for oxygen measurements at small scales and high gradients by the suppression of the optical cross-talk effect present for conventional POs. Since the sensing layer is coated directly onto a glass surface, there is no oxygen diffusion within the support foil or imaging window to be taken into account. Further improvements could be made by incorporating light-harvesting molecules in the sensing matrix to enhance the brightness of the image (Mayr et al. 2009), which would allow the decrease of layer thickness to build faster sensors. Silanization of the FOFP before coating could be performed to optimize the adhesion of the sensing layer to the glass surface (Kühl et al. 2007). The overall mechanical complexity of the new setup is only slightly increased compared with conventional POs, and the optical system, electronics, and software are identical. Therefore, the implementation of the new method is straightforward.

The present FOFP setup provide suitable scalar irradiance measurements for the investigated sediment, however, the accuracy and applicability can be improved by using different coatings and filter setups. A white-scattering material as used for scalar irradiance microsensors (Lassen et al. 1992b) instead of the red-sensing layer would allow imaging of spectral composition of the light field, using different filter sets or hyperspectral imaging. Thus, wavelength-dependent light attenuation coefficients could be obtained. Such adaptations would however limit the combined oxygen-irradiance measurements. Rotating filters in front of the CCD camera and a mosaic-like structure of oxygen-sensing dye and white-scattering layer would allow performing both measurements, but would increase the overall measurement time and decrease the spatial resolution.

The principle of the HiPO can also be used together with in situ modules (Glud et al. 2001); the FOFP would then have to be inserted into the periscope of the module. This would enable studying oxygen dynamics in benthic phototrophic communities in sediments or microbial mats together with the changing light conditions due to diurnal cycles, cloud coverage, and sediment rearrangements by infauna.

A general aspect of all types of PO measurements that has to be considered is the fact that they act as an impermeable boundary within the sediment, disturbing the original oxygen and light distribution. Especially strong heterogeneities within the sediment are influenced and small features of elevated or reduced oxygen concentration are magnified by this effect. Furthermore, it should be noted that the DBL can be widened by the presence of the optode (Glud 2008). To broaden the applicability of our method, the use of fluorophores for other parameters is possible. To date, sensing chemistries for pH (Stahl et al. 2006), pCO_2 (Zhu et al. 2006), NH_4^+ (Strömberg and Hulth 2005), and temperature (Borisov et al. 2006) are available, which could be easily combined with the HiPO.

References

Bachar, A., L. Polerecky, J. P. Fischer, K. Vamvakopoulos, D. De Beer, and H. M. Jonkers. 2008. Two-dimensional mapping of photopigment distribution and activity of Chloroflexus-like bacteria in a hypersaline microbial mat. FEMS Microbiol. Ecol. 65:434-448 [doi:10.1111/j.1574-6941.2008.00534.x].

Barranguet, C., J. Kromkamp, and J. Peene. 1998. Factors controlling primary production and photosynthetic characteristics of intertidal microphytobenthos. Mar. Ecol. Prog. Ser. 173:117-126 [doi:10.3354/meps173117].

Bateson, M. M., and D. M. Ward. 1988. Photoexcretion and fate of glycolate in a hot spring cyanobacterial mat. Appl. Environ. Microbiol. 54:1738-1743.

Behrens, J. W., H. J. Stahl, J. F. Steffensen, and R. N. Glud. 2007. Oxygen dynamics around buried lesser sandeels *Ammodytes tobianus* (Linnaeus 1785): mode of ventilation and oxygen requirements. J. Exp. Biol. 210:1006 [doi:10.1242/jeb.000570].

Berner, R. 1980. Early diagenesis: a theoretical approach, 1st ed. Princeton Univ. Press.

Borisov, S. M., A. S. Vasylevska, C. Krause, and O. S. Wolfbeis. 2006. Composite luminescent material for dual sensing of oxygen and temperature. Adv. Funct. Mater. 16:1536-1542 [doi:10.1002/adfm.200500778].

Boudreau, B. P. 1997. Diagenetic models and their implementation: modelling transport and reactions in aquatic sediments. Springer.

Cai, L.-D. 1988. Some notes on repeated averaging smoothing. *In* J. Kittler [ed.], Pattern recognition: 4th international conference, Cambridge, U.K., March 28-30, 1988: proceedings. Springer-Verlag. p. 597-605. [doi:10.1007/3-540-19036-8_60].

Canfield, D. E., and others. 1993. Pathways of organic carbon oxidation in three continental margin sediments. Mar. Geol. 113:27-40 [doi:10.1016/0025-3227(93)90147-N].

Castenholz, R. W., B. B. Jorgensen, E. D'amelio, and J. Bauld. 1991. Photosynthetic and behavioral versatility of the cyanobacterium *Oscillatoira boryana* in a sulfide-rich microbial mat. FEMS Microbiol. Lett. 86:43-58 [doi:10.1111/j.1574-6968.1991.tb04794.x].

Crank, J. 1979. The mathematics of diffusion, 2nd ed. Oxford Univ. Press.

Cypionka, H. 2000. Oxygen respiration by desulfovibrio species. Annu. Rev. Microbiol. 54:827-848 [doi:10.1146/annurev.micro.54.1.827].

Dodds, W. K. 1992. A modified fiber-optic light microprobe to measure spherically integrated photosynthetic photon flux

density: characterization of periphyton photosynthesis-irradiance patterns. Limnol. Oceanogr. 37(4):871-878.

———, B. J. F. Biggs, and R. L. Lowe. 1999. Photosynthesis-irradiance patterns in benthic microalgae: variations as a function of assemblage thickness and community structure. J. Phycol. 35:42-53 [doi:10.1046/j.1529-8817.1999.3510042.x].

Epping, E. H. G., and B. B. Jørgensen. 1996. Light-enhanced oxygen respiration in benthic phototrophic communities. Mar. Ecol. Prog. Ser. 139:193-203 [doi:10.3354/meps139193].

———, A. Khalili, and R. Thar. 1999. Photosynthesis and the dynamics of oxygen consumption in a microbial mat as calculated from transient oxygen microprofiles. Limnol. Oceanog. 44:1936-1948.

Fenchel, T., and R. N. Glud. 2000. Benthic primary production and O2-CO2 dynamics in a shallow-water sediment: spatial and temporal heterogeneity. Ophelia 53:159-172.

Franke, U. 2005. Applications of planar oxygen optodes in biological aquatic systems. PhD thesis, University Bremen.

———, L. Polerecky, E. Precht, and M. Huettel. 2006. Wave tank study of particulate organic matter degradation in permeable sediments. Limnol. Oceanogr. 51:1084-1096.

Frederiksen, M. S., and R. N. Glud. 2006. Oxygen dynamics in the rhizosphere of *Zostera marina*: A two-dimensional planar optode study. Limnol. Oceanogr. 51:1072-1083.

Glud, R. N. 2008. Oxygen dynamics of marine sediments. Mar. Biol. Res. 4:243-289 [doi:10.1080/17451000801888726].

———, N. B. Ramsing, J. K. Gundersen, and I. Klimant. 1996. Planar optrodes: a new tool for fine scale measurements of two-dimensional O2 distribution in benthic communities. Mar. Ecol. Prog. Ser 140:217-226 [doi:10.3354/meps140217].

———, M. Kühl, O. Kohls, and N. Ramsing. 1999. Heterogeneity of oxygen production and consumption in a photosynthetic microbial mat as studied by planar optodes. J. Phycol. 35:270-279 [doi:10.1046/j.1529-8817.1999.3520270.x].

———, A. Tengberg, M. Kühl, P. O. J. Hall, I. Klimant, and G. Holst. 2001. An in situ instrument for planar O_2 optode measurements at benthic interfaces. Limnol. Oceanogr. 46:2073-2080.

———, F. Wenzhöfer, A. Tengberg, M. Middelboe, K. Oguri, and H. Kitazato. 2005. Distribution of oxygen in surface sediments from central Sagami Bay, Japan: In situ measurements by microelectrodes and planar optodes. Deep-Sea Res. I 52:1974-1987 [doi:10.1016/j.dsr.2005.05.004].

Hargrave, B. T. 1972. Aerobic decomposition of sediment and detritus as a function of particle surface area and organic content. Limnol. Oceanogr. 17:583-596.

Holst, G., O. Kohls, I. Klimant, B. König, M. Kühl, and T. Richter. 1998. A modular luminescence lifetime imaging system for mapping oxygen distribution in biological samples. Sens. Actuat. B: Chem. 51:163-170 [doi:10.1016/S0925-4005(98)00232-9].

———, and B. Grunwald. 2001. Luminescence lifetime imaging with transparent oxygen optodes. Sens. Actuat. B Chem. 74:78-90 [doi:10.1016/S0925-4005(00)00715-2].

———, U. Franke, and B. Grunwald. 2001. Transparent oxygen optodes in environmental applications at fine scale as measured by luminescence lifetime imaging. Proc. SPIE Int. Soc. Optic. Eng. 4576:138-148.

Jensen, S. T., M. Kühl, R. N. Glud, B. B. Jørgensen, and A. Priemé. 2005. Oxic microzones and radial oxygen loss from roots of *Zostera marina*. Mar. Ecol. Prog. Ser. 293:49-58 [doi:10.3354/meps293049].

Jørgensen, B. B., and N. P. Revsbech. 1985. Diffusive boundary layers and the oxygen uptake of sediments and detritus. Limnol. Oceanogr. 30:111-122 [doi:10.4319/lo.1985.30.1.0111].

———, and D. J. Des Marais. 1986. A simple fiber-optic microprobe for high resolution light measurements: application in marine sediment. Limnol. Oceanogr. 31:1376-1383 [doi:10.4319/lo.1986.31.6.1376].

Koenderink, J. 1984. The structure of images. Biol. Cybern. 50:363-370 [doi:10.1007/BF00336961].

König, B., O. Kohls, G. Holst, R. N. Glud, and M. Kühl. 2005. Fabrication and test of sol–gel based planar oxygen optodes for use in aquatic sediments. Mar. Chem. 97:262-276 [doi:10.1016/j.marchem.2005.05.003].

Kühl, M., and B. B. Jørgensen. 1992. Spectral light measurements in microbenthic communities with a fiber-optic microprobe coupled to a sensitive diode array detector system. Limnol. Oceanogr 37:1813–1823.

———, and B. B. Jørgensen. 1994. The light field of microbenthic communities: radiance distribution and microscale optics of sandy coastal sediments. Limnol. Oceanogr. 39:1368-1398.

———, C. Lassen, and B. B. Jørgensen. 1994. Light penetration and light intensity in sandy marine sediments measured with irradiance and scalar irradiance fiber-optic microprobes. Mar. Ecol. Prog. Ser. 105:139-148 [doi:10.3354/meps105139].

———, L. Rickelt, and R. Thar. 2007. Combined imaging of bacteria and oxygen in biofilms. Appl. Environ. Microbiol. 73:6289-6295 [doi:10.1128/AEM.01574-07].

———, and L. Polerecky. 2008. Functional and structural imaging of phototrophic microbial communities and symbioses. Aquat. Microb. Ecol. 53:99-118 [doi:10.3354/ame01224].

———, G. Holst, A. W. D. Larkum, and P. Ralph. 2008. Imaging of oxygen dynamics within the endolithic algal community of the massive coral porites lobata. J. Phycol. 44:541-550 [doi:10.1111/j.1529-8817.2008.00506.x].

Lassen, C., H. Ploug, and B. B. Jorgensen. 1992a. Microalgal photosynthesis and spectral scalar irradiance in coastal marine sediments of Limfjorden, Denmark. Limnol. Oceanog. 37:760-772.

———, H. Ploug, and B. B. Jørgensen. 1992b. A fibre-optic scalar irradiance microsensor: application for spectral light measurements in sediments. FEMS Microbiol. Ecol. 86:247-254 [doi:10.1111/j.1574-6968.1992.tb04816.x].

———, R. N. Glud, N. B. Ramsing, and N. P. Revsbech. 1998. A method to improve the spatial resolution of photosynthetic rates obtained by oxygen microsensors. J. Phycol. 34:89-93 [doi:10.1046/j.1529-8817.1998.340089.x].

Macintyre, H., and J. Cullen. 1995. Fine-scale vertical resolution of chlorophyll and photosynthetic parameters in shallow-water benthos. Mar. Ecol. Prog. Ser. 122:227-237 [doi:10.3354/meps122227].

Mayr, T., S. M. Borisov, T. Abel, B. Enko, K. Waich, G. N. Mistlberger, and I. Klimant. 2009. Light harvesting as a simple and versatile way to enhance brightness of luminescent sensors. Anal. Chem. 81:6541-6545 [doi:10.1021/ac900662x].

Middelburg, J. J., C. M. Duarte, and J. P. Gattuso. 2005. Respiration in coastal benthic communities. Resp. Aquat. Ecosys. 1:206-225.

Oguri, K., H. Kitazato, and R. N. Glud. 2006. Platinum octaetylporphyrin based planar optodes combined with an UV-LED excitation light source: An ideal tool for high-resolution O-2 imaging in O-2 depleted environments. Mar. Chem. 100:95-107 [doi:10.1016/j.marchem.2005.11.005].

Pamatmat, M. M. 1971. Oxygen consumption by the seabed. IV. Shipboard and laboratory experiments. Limnol. Oceanogr. 16:536-550.

Perkins, R., G. Underwood, V. Brotas, G. Snow, B. Jesus, and L. Ribeiro. 2001. Responses of microphytobenthos to light: primary production and carbohydrate allocation over an emersion period. Mar. Ecol. Prog. Ser. 223:101-112 [doi:10.3354/meps223101].

Ploug, H., C. Lassen, and B. B. Jørgensen. 1993. Action spectra of microalgal photosynthesis and depth distribution of spectral scalar irradiance in a coastal marine sediment of Limfjorden, Denmark. FEMS Microbiol. Ecol. 102:261-270 [doi:10.1111/j.1574-6968.1993.tb05817.x].

Poulsen, L., and P. R. Ogilby. 2000. Oxygen diffusion in glassy polymer films: effects of other gases and changes in pressure. J. Phys. Chem. A 104:2573-2580 [doi:10.1021/jp993449r].

Precht, E., U. Franke, L. Polerecky, and M. Huettel. 2004. Oxygen dynamics in permeable sediments with wave-driven pore water exchange. Limnol. Oceanogr. 49:693-705.

Revsbech, N. P., B. B. Jørgensen, and O. Brix. 1981. Primary production of microalgae in sediments measured by oxygen microprofile, H 14 CO 3-fixation, and oxygen exchange methods. Limnol. Oceanogr. 26:717-730.

———, and B. B. Jørgensen. 1983. Photosynthesis of benthic microflora measured with high spatial resolution by the oxygen microprofile method: capabilities and limitations of the method. Limnol. Oceanogr. 28:749-756 [doi:10.4319/lo.1983.28.4.0749].

———, B. Madsen, and B. B. Jørgensen. 1986. Oxygen production and consumption in sediments determined at high spatial resolution by computer simulation of oxygen microelectrode data. Limnol. Oceanogr. 31:293-304.

Saburova, M., A., and G. I. Polikarpov. 2003. Diatom activity within soft sediments: behavioural and physiological processes. Mar. Ecol. Prog. Ser. 251:115-126 [doi:10.3354/meps251115].

Serôdio, J., S. Vieira, S. Cruz, and F. Barroso. 2005. Short-term variability in the photosynthetic activity of microphytobenthos as detected by measuring rapid light curves using variable fluorescence. Mar. Biol. 146:903-914 [doi:10.1007/s00227-004-1504-6].

Stahl, H., A. Glud, C. R. Schroder, I. Klimant, A. Tengberg, and R. N. Glud. 2006. Time-resolved pH imaging in marine sediments with a luminescent planar optode. Limnol. Oceanogr. Methods 4:336-345.

Stockdale, A., W. Davison, and H. Zhang. 2009. Micro-scale biogeochemical heterogeneity in sediments: A review of available technology and observed evidence. Earth Sci. Rev. 92:81-97 [doi:10.1016/j.earscirev.2008.11.003].

Strömberg, N., and S. Hulth. 2005. Assessing an imaging ammonium sensor using time correlated pixel-by-pixel calibration. Anal. Chim. Acta 550:61-68 [doi:10.1016/j.aca.2005.06.074].

Underwood, G. J. C., R. G. Perkins, M. C. Consalvey, A. R. M. Hanlon, K. Oxborough, N. R. Baker, and D. M. Paterson. 2005. Patterns in microphytobenthic primary productivity: species-specific variation in migratory rhythms and photosynthetic efficiency in mixed-species biofilms. Limnol. Oceanogr. 50:755-767.

Wenzhöfer, F., and R. N. Glud. 2004. Small-scale spatial and temporal variability in benthic O_2 dynamics of coastal sediments: Effects of fauna activity. Limnol. Oceanogr 49:1471-1481.

Zhou, Z., R. Shinar, A. J. Allison, and J. Shinar. 2007. Enhanced photoluminescence of oxygen sensing films through doping with high dielectric constant particles. Adv. Funct. Mater. 17:3530-3537 [doi:10.1002/adfm.200700324].

Zhu, Q. Z., R. C. Aller, and Y. Z. Fan. 2006. A new ratiometric, planar fluorosensor for measuring high resolution, two-dimensional pCO(2) distributions in marine sediments. Mar. Chem. 101:40-53 [doi:10.1016/j.marchem.2006.01.002].

Submitted10 September 2009
Revised 12 March 2010
Accepted 31 March 2010